Supporting Information

A High Stability Polyoxometalate-Based Metal-Organic Framework with ABW Zeolite-Like Structure

Xiao-Xin Li,[a†] Feng-Cui Shen,[b, c†] Jiang Liu,[b] Shun-Li Li,[b] Long-Zhang Dong,[b] Qiang Fu,[a] Zhong-Min Su*[a] and Ya-Qian Lan*[b]

[a]Institute of Functional Material Chemistry, Department of Chemistry, National & Local United Engineering Lab for Power Battery, Northeast Normal University, Changchun 130024, P. R. China

[b]Jiangsu Key Laboratory of Biofunctional Materials, School of Chemistry and Materials Science, Nanjing Normal University, Nanjing 210023, P. R. China

[c]School of Biological and Chemical Engineering, Anhui Polytechnic University, Wuhu 241000 P. R. China

[‡] These authors contributed to this work equally.

Corresponding Author: yqlan@njnu.edu.cn; zmsu@nenu.edu.cn.

S1. Materials and measurements

All starting materials, reagents and solvents used in experiments were commercially available, high-grade purity materials and used without further purification. Sodiummolybdate dehydrate ($Na_2MoO_4·2H_2O$, 99%), Molybdenum Powder (Mo, 99.95%), Hydrochloric acid (HCl, 36%) and 1,4-dicarboxybenzene acid (1,4-H_2bdc, 99%) were purchased from Sinopharm Chemical Reagent Co. Ltd. Zinc chloride ($ZnCl_2$, 98.0%) was purchased from Shanghai Xinbao Fine Chemical Factory. Tetrabutylammonium Hydroxide (TBAOH, 25% in methanol) was purchased from Aladdin. Phosphorous acid (H_3PO_3, 99%) was purchased from Jiangsu Yonghua Chemical Technology Reagent Co. Ltd, 1,2,3-Benzotrialole (1,2,3-bzt, 99.45%) was purchased from Tokyo Chemical Industry Co. Ltd.

Analytical techniques

Thermogravimetric analyses (TGA) of the sample was performed on a Perkin–Elmer TG-7 analyzer heated from room temperature to 1000 °C in flowing N_2/O_2 with a heating rate of 10 °C/min. Fourier transform infrared spectroscopy (FTIR) was recorded in the range of 4000-400 cm^{-1} on a Mattson Alpha-Centauri spectrometer using the technique of pressed KBr pellets. Powder X-Ray diffraction (PXRD) measurements were recorded ranging from 3 to 50° at room temperature on a D/max 2500 VL/PC diffractometer (Japan) with equipped with graphite mono-chromatized Cu Kα radiation (λ = 1.54060 Å). X-ray photoelectron spectroscopy (XPS) was collected on scanning X-ray microprobe (PHI 5000 Verasa, ULAC-PHI, Inc.) using Al kα radiation and the C1s peak at 284.8 eV as internal standard. Nitrogen adsorption-desorption isotherms were measured at 77 K on a Quantachrome Instruments Autosorb AS-6B.

Electrochemistry

Super P carbon and the sample were ground together and mixed with the polyvinylidene fluoride (PVDF) binder in N-methyl-2-pyrrolidinone (NMP) solvent to form slurry. The final mixture consisted of 60% active material, 30% super P carbon and 10% PVDF binder. The slurry was deposited onto copper foils and dried under a vacuum at 60 °C for 24 h. Coin type cells were assembled in a glove box under argon gas atmosphere, with oxygen and water concentration maintained below 1 ppm, where the lithium metal anode was separated by a Whatman glass fiber membrane. 1 M $LiPF_6$ dissolved in a mixture of ethylene carbonate (EC) and diethyl carbonate (DEC) (1:1 v/v) was served as electrolyte. Before electrochemical tests, the batteries were soaked overnight.

The cells were disassembled in the glove box after discharged at a constant current of 100 mA g^{-1} to 0.01 V. The working electrode was washed with DMC several times before vacuum drying for 12 h at room temperature. Then it was scraped off the Cu foil for XPS tests.

Single-crystal X-ray diffraction

Single crystal X-Ray intensity data collection was carried out at room temperature with a Bruker Nonius X8 APEX 2 diffractometer, equipped with a CCD bidimensional detector using the monochromatized wavelength (Mo Ka) = 0.71073 Å. The absorption correction was based on multiple and symmetry equivalent reflections in the data set using the SADABS program based on the method of Blessing. The structure was solved direct methods and refined by full-matrix least squares using the SHELX-TL package. Lorentz-polarization and absorption corrections were applied.

S2. Synthesis of TBA$_{5/2}$[PMo$^V_8$Mo$^{VI}_4$O$_{37}$(OH)$_3$Zn$_4$(bdc)$_{1/2}$(bzt)$_{3/2}$]·3/2H$_2$O (NENU-601)

A mixture of Na$_2$MoO$_4$·2H$_2$O (0.630 g, 2.60 mmol), H$_3$PO$_3$(0.020 g, 0.25 mmol), ZnCl$_2$ (0.136 g, 1.00 mmol), 25 wt % TBAOH in methanol (400 μL, 0.375 mmol) and H$_2$O (7 mL) was stirring for two hours and the pH was adjusted to approximately 5.5 (pH$_i$) by the addition of 4 M HCl resulting in a milky white suspension. Then molybdenum powder (60 mg, 0.62 mmol), 1,4-bdc (0.0332g, 0.20 mmol) and 1,2,3-Bzt (0.0715 g, 0.60 mmol) was following dispersed into the aqueous suspension. Solution was mixed under vigorous stirring and ultrasounding for approximately 30 min, transferred and sealed in a 15 mL Teflon lined stainless-steel container maintaining at 180 °C for 72 h and then cooled to room temperature at a rate of 10°C·h^{-1}. The product was isolated by filtration and separated from an amorphous brown powder and dark red rhombus crystals of **NENU-601** by decantation, and then washed with Millipore water, which were collected in 40% yield based on H$_3$PO$_3$. FTIR: n (cm^{-1}) =2962 (m), 2877(m), 2372 (w), 2346 (w), 1594 (m), 1481 (m), 1357 (m), 1178 (w), 960 (s), 934 (s), 816 (sh), 780 (sh). CCDC reference number: 1555051
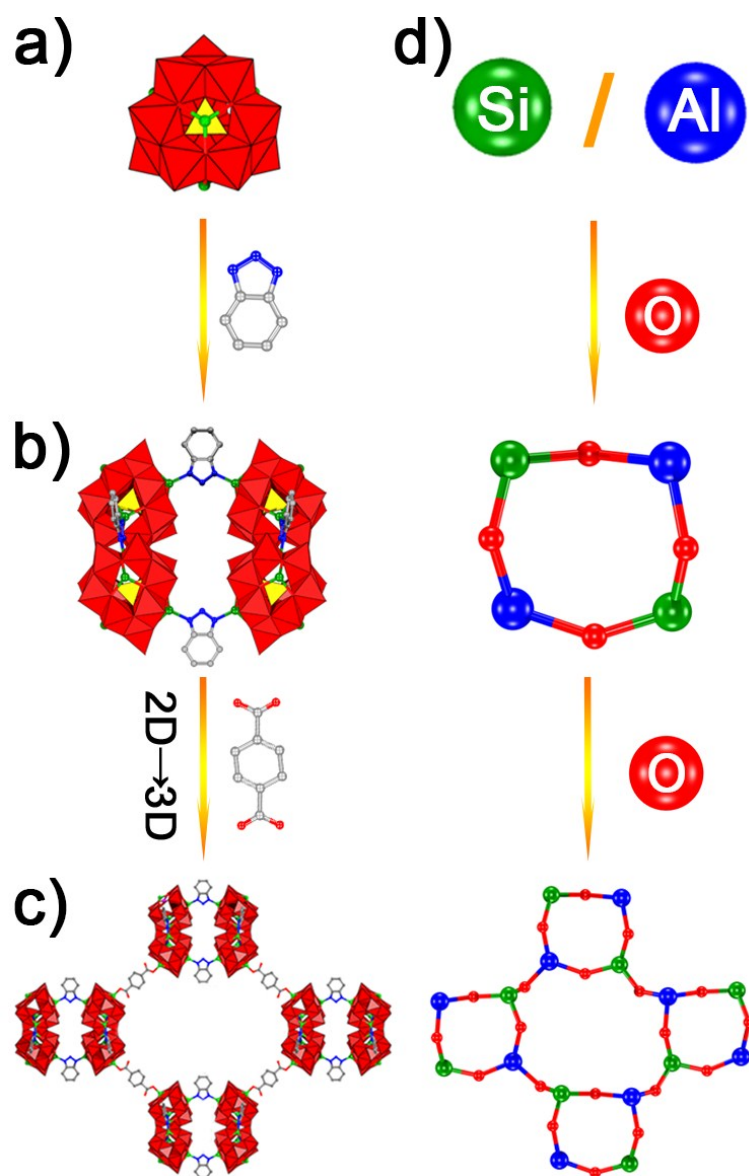
Fig. S1 Stepwise analysis of **NENU-601** by contrasting to ABW zeolite-like topological structure. (a) Wires or stick representation of the structure of ε-{Zn$_4$PMo$_{12}$O$_{40}$} cluster. (b) Schematic view of 2D layer in **NENU-601**. (c) Schematic view of 3D structure in **NENU-601**. (d) ABW zeolite structure.[1]
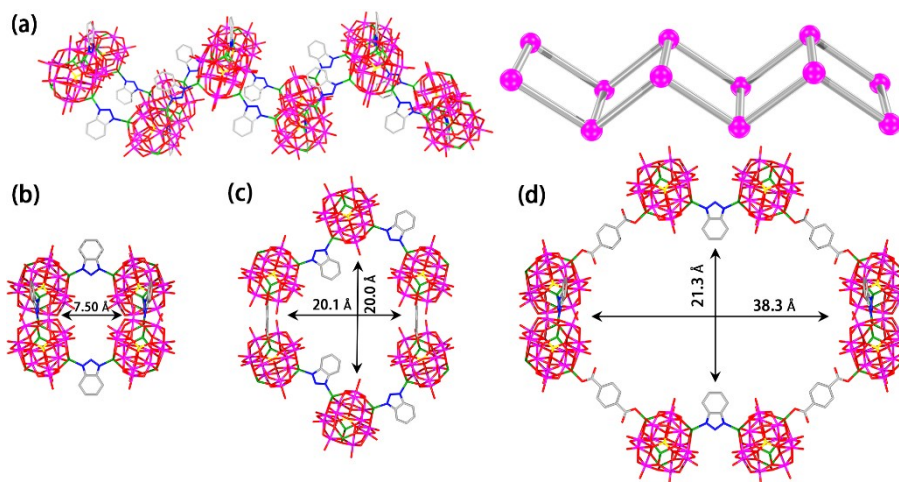
Fig. S2 Schematic view and dimension of **NENU-601**. (a) a double-sawtooth chain and its topology along *c* axis. (b)-(d) 4-, 6- and 8-rings of **NENU-601**, respectively.

Along the *c* axis, ε-$\{Zn_4PMo_{12}O_{40}\}$ can be regarded as a SBU in which three of four Zn ions coordinating bzt$^-$ ligands construct a double-sawtooth chain. The chains are further linked by the bdc^{2-} ligands, resulting in a 3D network with rhombus channels, 8-rings nanosized dimensions of 21.3 Å × 38.3 Å and 4-rings (7.5 Å × 7.5 Å) along *a* axis and 6-rings (20.0 Å × 20.1 Å) along *c* axis, respectively.
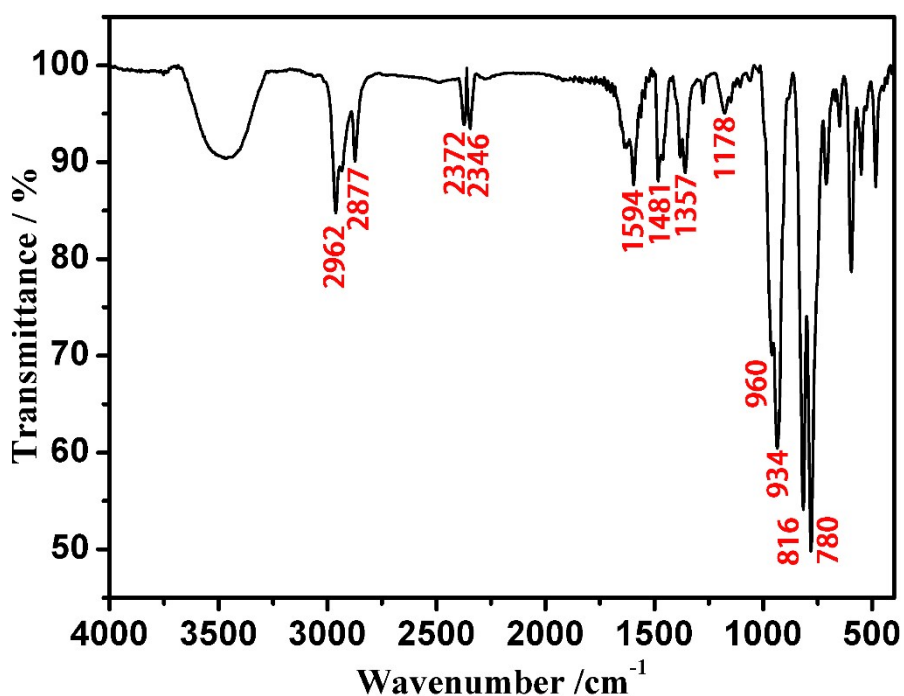
Fig. S3 The FTIR curve of **NENU-601**. Characteristic peaks of $[PMo^V_8Mo^{VI}_4O_{40}]^{11-}$ appeared on its spectrum: n (cm^{-1}) = 960 (s), 934 (sh), 816 (sh), 780 (sh). Characteristic peaks of v_{C-O} in carboxyl appeared on its spectrum: n (cm^{-1}) = 2372 (w), 2346 (w). The peak appearing at n (cm^{-1}) = 1178 (w) belongs to TBA$^+$ ions.
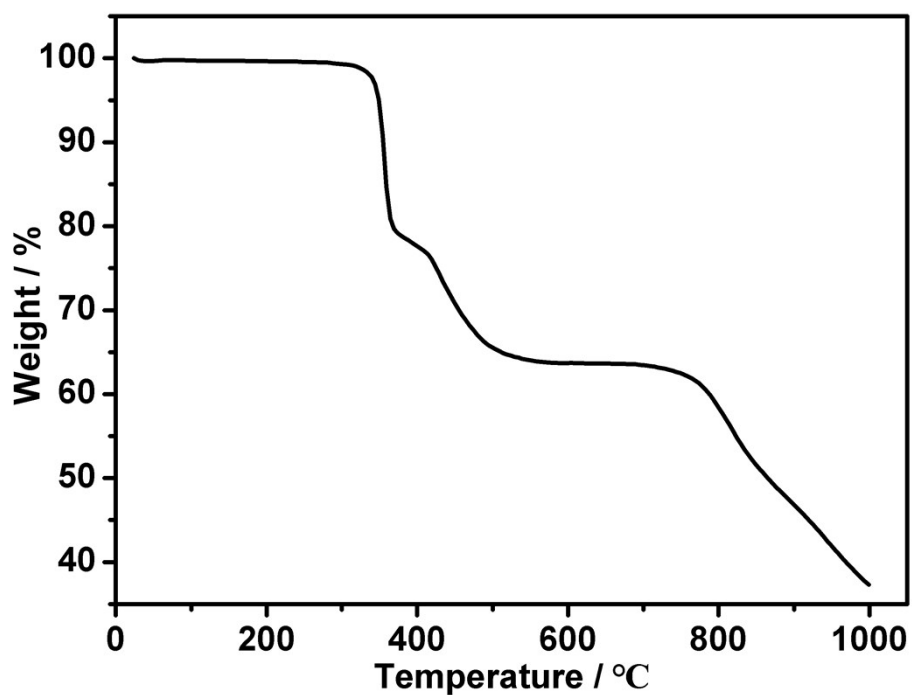
Fig. S4 The TGA curve of **NENU-601** measured in N_2/O_2 from room temperature to 1000 °C at the heating rate of 10 °C·min^{-1}.

The weight loss of **NENU-601** from room temperature to 300 °C is 0.8% corresponding to the loss of free water molecules. From 300 °C to 370 °C, the weight lost 20.02% immediately due to the splitting of TBA$^+$ ions with the calculated 20.04%. The framework gradually collapses from 370 °C to 570 °C in conformity with the release of bdc^{2-} and bzt$^-$ ligands (16.08% in reality and 17.4% in the calculation).
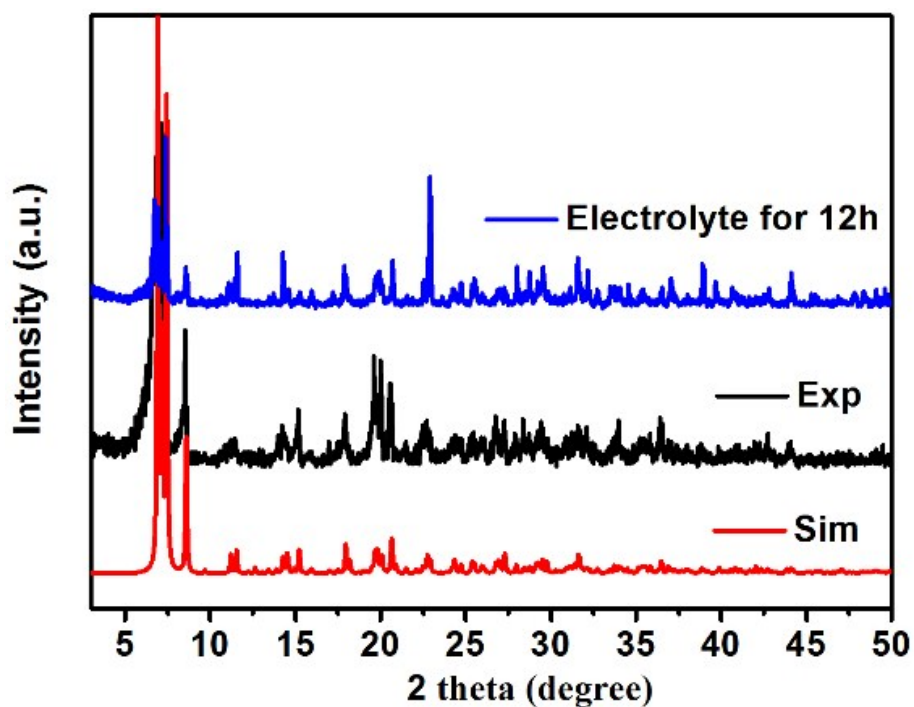
Fig. S5 The PXRD pattern of **Z-POMOF1**: simulated pattern (red), as-synthesized sample (black), electrolyte for 12h (blue), respectively.

Fig. S6 Nyquist plots of the **NENU-601** and **Z-POMOF1** as anode materials before and after battery cycling, respectively. (Inset: Randles equivalent circuit for the **NENU-601** and **Z-POMOF1** electrode/electrolyte interface) R1: electronic resistance of the electrodes and electrolyte; R2: charge transfer resistance; W1: Warburg impedance

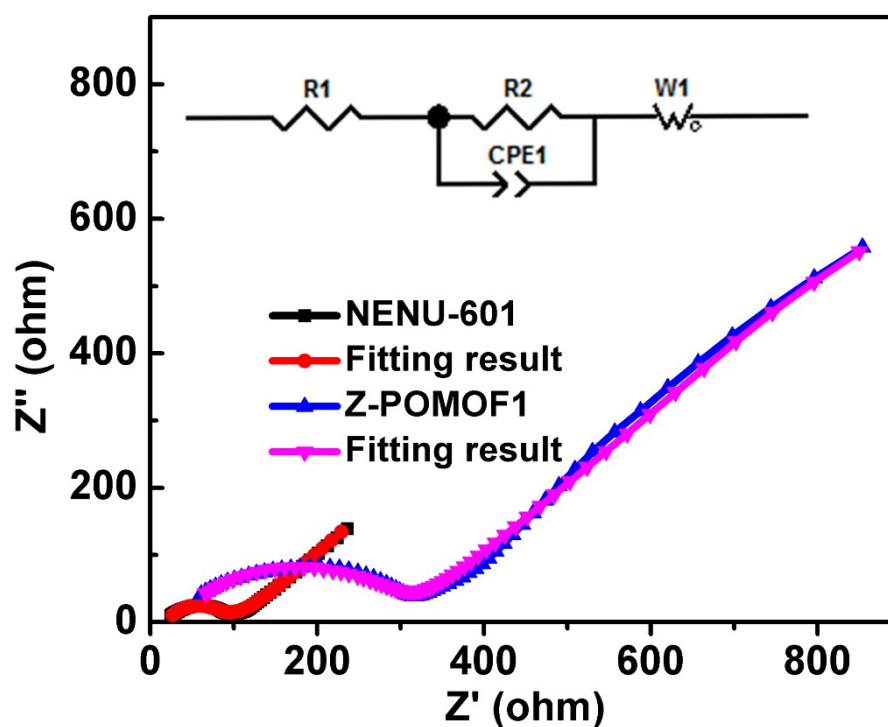related to the diffusion of lithium ions into the bulk electrodes. CPE: constant phase element.

We choose **Z-POMOF1** with the ligands of H_2bdc for the comparison, whose crystal structure is similar to the **NENU-601** with mixed ligands of Hbzt and H_2bdc. **Z-POMOF1** gets a capacity of 545 mAh g^{-1} under the same testing situation after 100 cycles. To further confirm the contribution of ligands to the capacity, we tested electrical performance of the ligands Hbzt and H_2bdc as the anodes of LIBs in Fig 4b. The capacity was delivered up to the 216 mAh g^{-1} and 148 mAh g^{-1}, respectively. So **NENU-601** has more superior performance than **Z-POMOF1** partly originating from the contribution of N-containing ligands Hbzt whose uncoordinated nitrogen atom can interact with lithium ions. Furthermore, we carried out the EIS spectroscopy to investigate the reaction kinetics of **NENU-601** and **Z-POMOF1** in Fig. S6. Apparently, **NENU-601** has a small diameter meaning the low ion and mass transfer resistance. As a result, the contribution of N-containing ligands Hbzt and the lower impedance are responsible for the better lithium ion storage property of **NENU-601** than that of **Z-POMOF1**.

To further study the mechanism of our zeolite-like crystalline for LIBs, the XPS survey spectrum was conducted to research the changes of valence states of transition metal before and after discharge in the batteries.[3-10] Before the discharge of the cell, the Mo 3d spectrum shows two main peaks at 231.3 eV and 234.5 eV which can be deconvoluted into four peaks at 234.2 eV, 231.1 eV, 235.1 eV and 232.1 eV, respectively, ascribed to Mo^{5+} $3d_{3/2}$ and Mo^{5+} $3d_{5/2}$, Mo^{6+} $3d_{3/2}$ and Mo^{6+} $3d_{5/2}$. However, after discharging to 0.01 V, the existence of Mo^{4+} can be discovered in the binding energy of 232.2 eV. As showed in Fig. S7c, two peaks of Zn $2p_{3/2}$ and Zn $2p_{1/2}$ at 1022.5 eV and 1045.5 eV in Zn 2p prove the existence of Zn^{2+}, while the shifting and separation of the binding energy indicate the partial production of Zn^0 after discharging to 0.01 V. Both valence changes of Mo and Zn demonstrate the redox reaction of $[Zn_4 PMo^V_8Mo^{VI}_4O_{40}]^{3-}$ ions in LIBs.
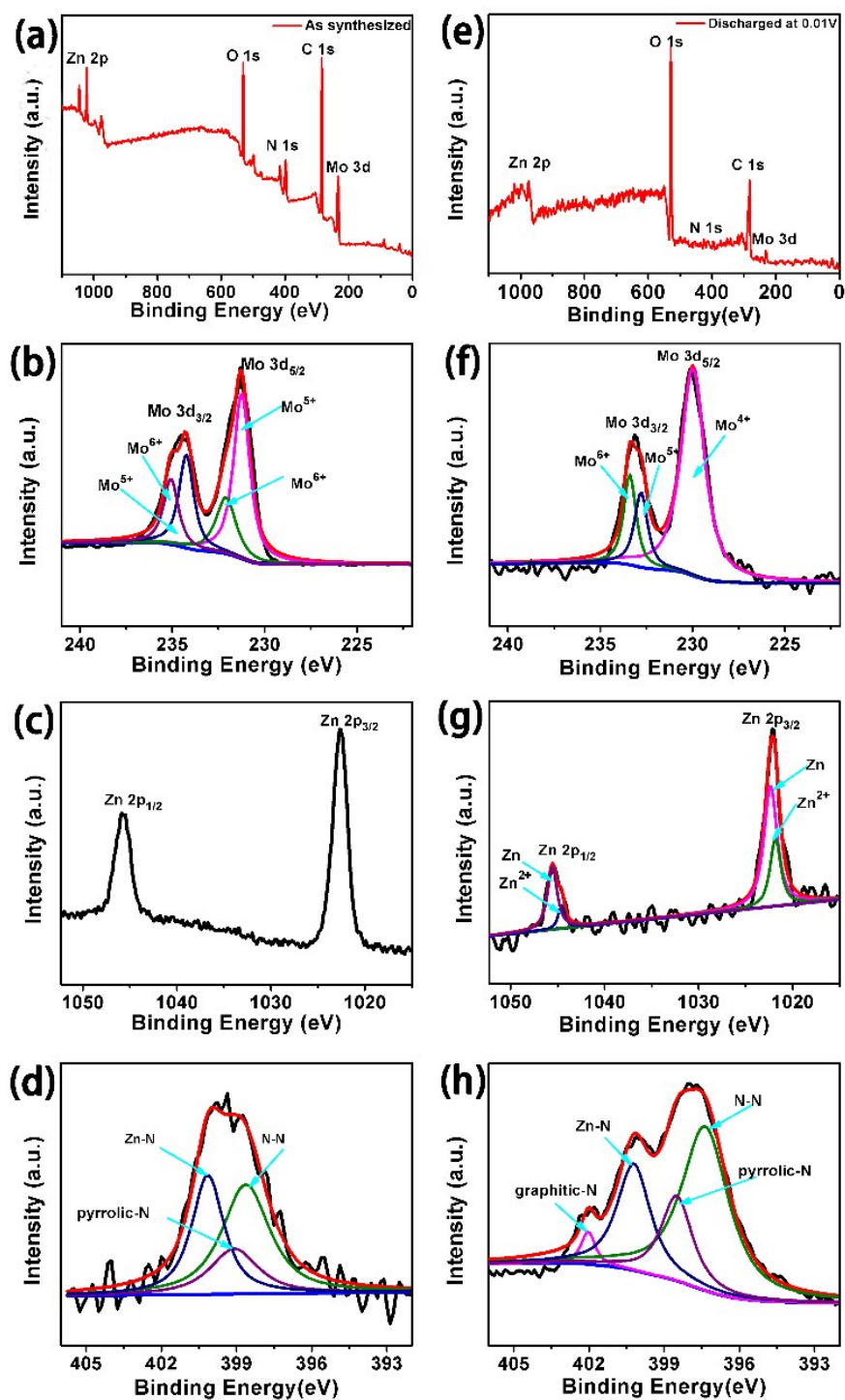
Fig. S7 XPS spectra of **NENU-601** before and after discharged at 0.01 V. (a) - (d): As synthesized powders. (a) Survey scan, (b) Mo 3d, (c) Zn 2p, (d) N 1s, (e) - (f): Discharged at 0.01 V. (e) Survey scan, (f) Mo 3d, (g) Zn 2p, (h) N 1s, respectively.
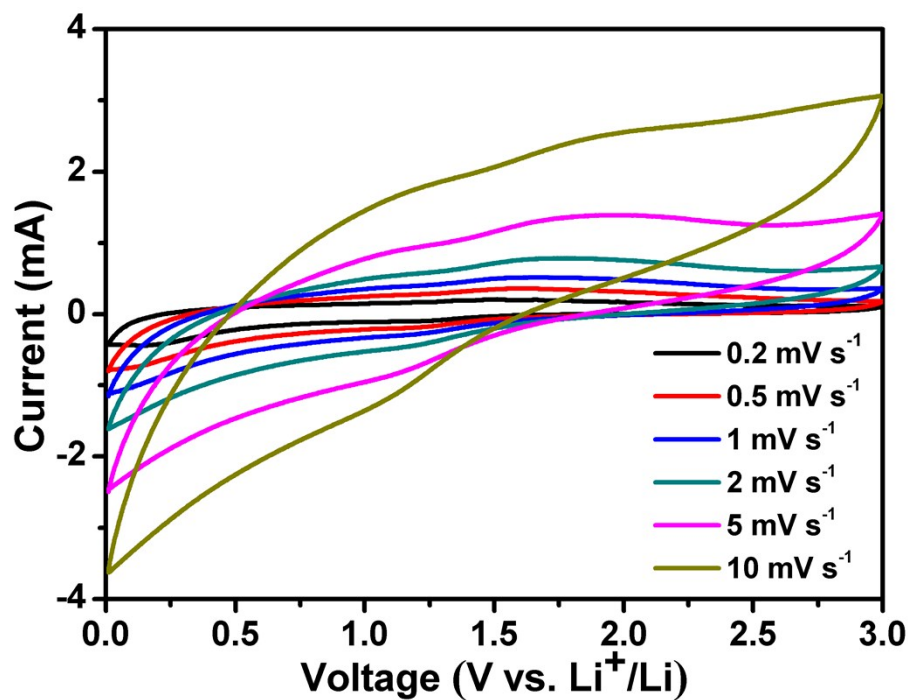
Fig. S8 CV curves of **NENU-601** at various scan rates, from 0.2 to 10 mV s^{-1}.
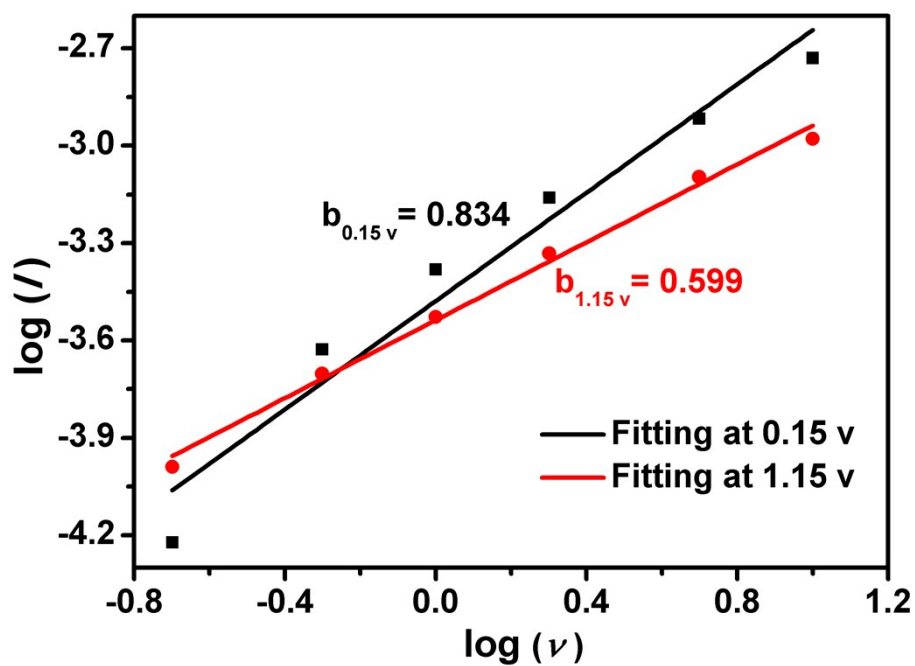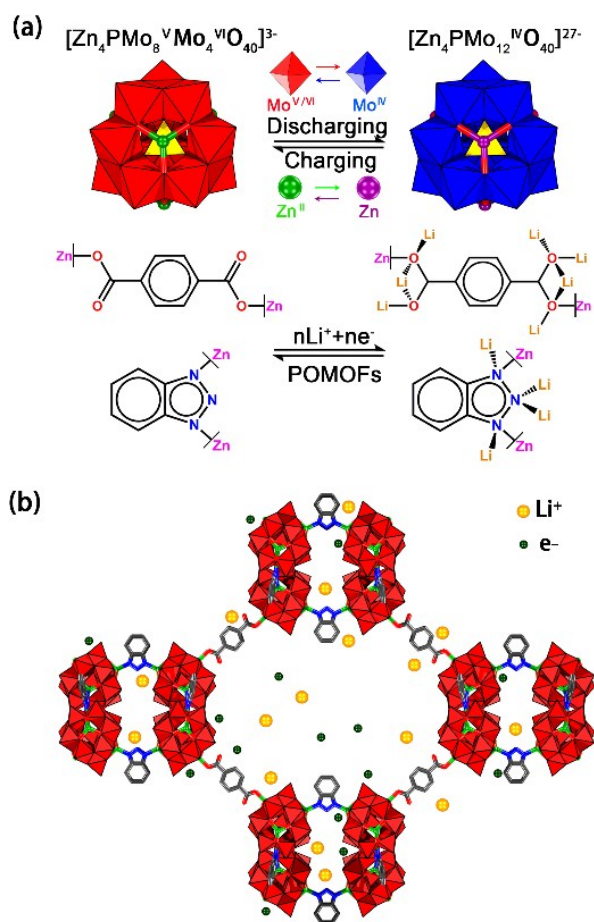

Fig. S9 b-value determination of 1.15 V and 0.15 V cathodic current, respectively.

Fig. S10 Schematic diagrams of the possible mechanism for the capacity of **NENU-601**. (a) The battery behaviours of N in Hbzt and O in H_2bdc coordinate with Li^+ and redox of metal ions (Mo and Zn) in the POMs, respectively. (b) The capacitive behavior in addition to the lithium ions and electrons insert into the lattice of **NENU-601**.

We found that the experimental capacity (770 mAh g^{-1}) is higher than the theoretical value (about 360 mAh g^{-1}) determined from: (1) Redox reactions where Zn^{2+} transformed into Zn and Mo^{6+}/Mo^{5+} transformed into Mo^{4+} occured in $[Zn_4PMo^V_8Mo^{VI}_4O_{40}]^{3-}$ ion because of the intercalation mechanism for Li storage. (2) Possible lithiation/delithiation sites for coordination with Li such as the uncoordinated N in Hbzt and O in H_2bdc ligands of **NENU-601**. The access capacity here possibly is the capacitive contribution derived from the pores of **NENU-601**. To support our thesis, CV profiles of **NENU-601** at different scan rates (0.2 - 10 mV s^{-1}) were recorded between 0.01 - 3.0 V (Fig. S8) to confirm the contribution of capacitive behavior. We explained it by the power law $i = av^b$ in which v is the scan rate, a and b are regulable parameters. Under normal conditions, $b = 0.5$ means the electrode reaction is diffusion-controlled and satisfies Cottrell's equation: $i = av^{0.5}$, while $b = 1$ represents the reaction is limited by a surface process. The parameter b can be calculated based on the slope of the linear graph of log i versus log v. While the scan rate is gradually

increased from 0.2 to 10 mV s^{-1}, the b value is calculated to be 0.599 at 1.15 V, signifying the main contribution of the diffusion-controlled lithium storage process. When it comes to 0.15 V, the b value is 0.834 (Fig. S9) manifesting the joint contribution. The mixed mechanism shows the total capacity of **NENU-601** originates from two parts (Fig. S10) agree with our speculation.
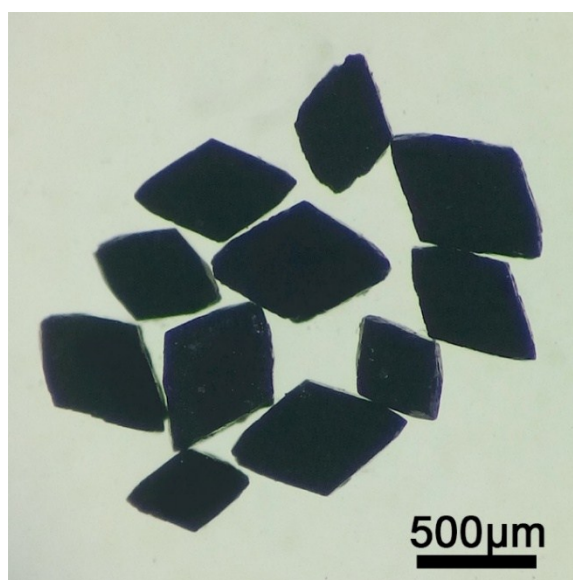
Fig. S11 The images of **NENU-601** under optical microscope.

Table S1 Crystal data and structure refinement for the compound.

	NENU-601
Empirical formula	$C_{26}H_{20}Mo_{24}N_9O_{87}P_2Zn_8$
Formula weight	2461.34
Crystal system	Orthorhombic
Space group	*Ibam*
***a* (Å)**	20.175(16)
***b* (Å)**	38.738(3)
c (Å)	52.010(4)
***α* (°)**	90.000(5)
β (°)	90.000(5)
***γ* (°)**	90.000(5)
***V* (Å³)**	40648(6)
Z	8
***D*$_{calc}$(g·cm^{-3})**	1.550
Abs.coeff.(mm^{-1})	2.421
***F*(000)**	17752
Reflns collected	109435/18225
GOFon *F*^{2}	1.043
***R*$_{int}$**	0.0354
***R*$_1$[a]**	0.0816
***wR*$_2$(all data)[b]**	0.1768

[a]$R_1=\Sigma||F_o|-|F_c||/\Sigma|F_o|$. [b]$wR_2=|\Sigma w\,(|F_o|^2-|F_c|^2)|/\Sigma|w(F_o^2)^2|^{1/2}$

Table S2 Selected bond distance (Å) of **NENU-601**.

Atom1	Atom2	Length/Å	Atom1	Atom2	Length/Å
P1	O2	1.559(5)	P1	O1	1.543(5)
P1	O4	1.549(5)	P1	O3	1.533(6)
Mo1	O1	2.631(5)	Mo7	O3	2.589(5)
Mo1	O8	2.009(6)	Mo7	O12	1.970(7)
Mo1	O7	1.996(6)	Mo7	O15	1.956(6)
Mo1	O19	1.812(6)	Mo7	O23	2.034(7)
Mo1	O17	1.814(6)	Mo7	O24	1.917(7)
Mo1	O29	1.701(7)	Mo7	O35	1.672(6)
Mo2	O1	2.490(5)	Mo8	O8	2.013(5)
Mo2	O10	1.956(6)	Mo8	O3	2.580(6)
Mo2	O9	1.968(6)	Mo8	O7	2.020(6)
Mo2	O18	2.055(6)	Mo8	O23	1.818(6)
Mo2	O17	2.014(6)	Mo8	O25	1.798(7)
Mo2	O30	1.657(6)	Mo8	O36	1.692(7)
Mo3	O1	2.498(5)	Mo9	O3	2.589(5)
Mo3	O5	1.961(6)	Mo9	O13	1.996(6)
Mo3	O6	1.927(7)	Mo9	O16	1.970(7)
Mo3	O18	2.061(6)	Mo9	O25	2.057(7)
Mo3	O19	2.022(7)	Mo9	O24	1.941(6)
Mo3	O31	1.664(6)	Mo9	O37	1.661(7)
Mo4	O2	2.498(5)	Mo10	O4	2.576(5)
Mo4	O5	1.956(6)	Mo10	O13	1.964(6)
Mo4	O6	1.952(6)	Mo10	O16	1.974(6)
Mo4	O20	2.064(7)	Mo10	O27	2.027(7)
Mo4	O21	2.005(6)	Mo10	O26	2.004(6)
Mo4	O32	1.663(7)	Mo10	O38	1.660(6)
Mo5	O2	2.561(6)	Mo11	O4	2.570(5)
Mo5	O14	1.993(6)	Mo11	O14	2.008(6)
Mo5	O11	1.992(6)	Mo11	O11	2.010(6)
Mo5	O22	1.796(6)	Mo11	O28	1.803(5)
Mo5	O21	1.825(6)	Mo11	O27	1.791(6)
Mo5	O33	1.668(7)	Mo11	O39	1.685(6)
Mo6	O2	2.587(5)	Mo12	O4	2.508(5)
Mo6	O20	2.088(7)	Mo12	O10	1.972(6)
Mo6	O12	1.951(6)	Mo12	O9	1.965(6)
Mo6	O22	2.007(7)	Mo12	O28	2.031(6)
Mo6	O15	1.957(7)	Mo12	O26	1.993(6)
Mo6	O34	1.659(6)	Mo12	O40	1.664(6)
Zn1	O6	1.994(7)	Zn3	O8	1.939(5)
Zn1	O12	1.962(6)	Zn3	O9	1.954(6)

Zn1	O7	1.940(6)	Zn3	O13	1.940(6)
Zn1	O41	1.922(6)	Zn3	N4	2.009(7)
Zn2	O14	1.946(6)	Zn4	O10	1.966(6)
Zn2	O16	1.936(7)	Zn4	O11	1.950(6)
Zn2	O15	1.963(6)	Zn4	O5	1.977(6)
Zn2	N3	1.970(7)	Zn4	N1	1.969(7)

Table S3 The BVS calculation result of P, Mo and Zn atoms in **NENU-601**.

Code	Bond Valence	Code	Bond Valence
P1	4.848	Mo1	6.010
Zn1	2.038	Mo2	5.315
Zn2	2.038	Mo3	5.334
Zn3	2.005	Mo4	5.319
Zn4	1.974	Mo5	6.264
		Mo6	5.252
		Mo7	5.448
		Mo8	6.052
		Mo9	5.311
		Mo10	5.297
		Mo11	6.200
		Mo12	5.327

Table S4 Comparison of **NENU-601** with other porous materials as the LIBs anode.

Materials	AMR (%)	RC/Cycles	CD (mA g^{-1})	CC/DC (mA h g^{-1})	Ref
NENU-601	60	780/200	100	626.6/1389	This work
POMOF-1	65	350/500	1.25C	720/1421	[11]
MOF177	85	--/50	100	110/425	[12]
NENU-507	50	640/100	100	566/1008	[13]
Li/Ni-NTC	60	482/80	100	601/1084	[14]
Zn(IM)$_{1.5}$(abIM)$_{0.5}$	70	190/200	100	--	[15]
Fe/Co-BTC	70	639/70	200	568.5/859.1	[16]
Co$_2$(OH)$_2$(bdc)	70	650/100	50	1005/1385	[17]

RC: Reversible capacity. CD: Current density. AMR: Active material ratio.

References

1. T. T. Ong, P. Kavuru, T. Nguyen, R. Cantwell, Ł. Wojtas and M. J. Zaworotko, *J. Am. Chem. Soc.*, 2011, **133**, 9224-9227.
2. F. Zheng, Y. Yang and Q. Chen, *Nat. Commun.*, 2014, **5**, 5261-5270.
3. B. Chen, R. Li, G. Ma, X. Gou, Y. Zhu and Y. Xia, *Nanoscale*, 2015, **7**, 20674-20684.
4. H. Wang, S. Zhuo, Y. Liang, X. Han and B. Zhang, *Angew. Chem. Int. Ed.*, 2016, **55**, 9055-9059.
5. J. Xie, Y. Zhang, Y. Han and C. Li, *ACS Nano*, 2016, **10**, 5304-5313.
6. C. E. Small, S. Chen, J. Subbiah, C. M. Amb, S. W. Tsang, T. H. Lai, J. R. Reynolds and F. So, *Nat. Photonics*, 2012, **6**, 115-120.
7. S. A. Wohlgemuth, R. J. White, M. G. Willinger, M. M. Titirici and M. Antonietti, *Green Chem.*, 2012, **14**, 1515-1523.
8. J. G. Choi and L. T. Thompson, *Appl. Surf. Sci.*, 1996, **93**, 143-149.
9. X. Wei, B. Man, M. Liu, C. Xue, H. Zhuang and C. Yang, *Phys. B: Condens. Matter*, 2007, **388**, 145-152.
10. Y. J. Tang, Y. Wang, X. L. Wang, S. L. Li, W. Huang, L. Z. Dong, C. H. Liu, Y. F. Li and Y. Q. Lan, *Adv. Energy Mater.*, 2016, **6**, 1606116.
11. Y. F. Yue, Y. C. Li, Z. H. Bi, G. M. Veith, C. A. Bridges, B. K. Guo, J. Chen, D. R. Mullins, S. P. Surwade, S. M. Mahurin, H. J. Liu, M. P. Paranthaman and S. Dai, *J. Mater. Chem. A*, 2015, **3**, 22989-22995.
12. X. X. Li, F. Y. Cheng, S. N. Zhang and J. Chen, J. Power Sources, 2006, **160**, 542–547.
13. Y. Y. Wang, M. Zhang, S. L. Li, S. R. Zhang, W. Xie, J. S. Qin, Z. M. Su and Y. Q. Lan, *Chem. Commun.*, 2017, **53**, 5204-5207.
14. X. Han, F. Yi, T. Sun and J. Sun, *Electrochem. Commun.*, 2012, **25**, 136-139.
15. Y. C. Lin, Q. J. Zhang, C. C. Zhao, H. L. Li, C. L. Kong, C. Shen and L. Chen, *Chem. Com-mun*, 2015, **51**, 697–699.
16. X. B. Xu, S. M. Chen, Y. F. Chen, H. Y. Sun, L. Song, W. He and X. Wang, *Small*, 2016, **12**, 2982-2990.
17. L. Gou, L. M. Hao, Y. X. Shi, S. L. Ma, X. Y. Fan, L. Xu, D. L. Li and K. Wang, *J. Solid State Chem*, 2014, **210***, 121-124.